*Int. J. Electrochem. Sci.*, 14 **(2019)** 10966 – 10982, doi: 10.20964/2019.12.10

International Journal of
ELECTROCHEMICAL
SCIENCE
www.electrochemsci.org

# Corrosion Inhibition of a Sol-Gel Coating Modified with Cobalt-Enriched Zeolite on AA2024-T3 Aluminum Alloy

*Bing Xue*[*], *Xuemei Zong, Can Wang, Huayuan Zhang, Jing Luo*

Jiangsu XCMG construction machinery research institute Ltd, 26# Tuolanshan RD, Gulou District, 221004, Xuzhou, Jiangsu, P.R.China.
[*]E-mail: xcmgxuebing@163.com

*Received:* 11 July 2019 / *Accepted:* 29 August 2019 / *Published:* 29 October 2019

Cobalt-enriched zeolite (CoNaX) nanocontainers, synthesized by ion-exchange reactions of zeolite X (NaX) and $Co(NO_3)_2$, were used as inhibitor additives to improve the corrosion protection of a sol-gel coating. A dispersion of CoNaX zeolite was uniform in the sol-gel coating and caused no defects. An increase in coating thickness was unapparent with the addition of CoNaX zeolite. Results of tests indicated that the corrosion protective properties of the sol-gel coating were remarkably improved. This was attributed to an enhanced cross-linking density by zeolite particles and a controlled release of $Co^{2+}$ in CoNaX zeolite. The released $Co^{2+}$ reacted with $OH^-$ from corrosion products, which formed a Co oxide/hydroxide precipitation. The precipitation covered defects and prevented contact of electrolyte with the substrate, which further slowed corrosion processes. CoNaX zeolite provided the coating with long-term inhibitive properties.

**Keywords:** zeolite; corrosion inhibitor; ion-exchange; sol-gel coating; electrochemistry

## 1. INTRODUCTION

AA2024-T3 aluminum alloy has been used as construction material in many industrial fields because of its high strength to weigh ratio and good mechanical properties [1,2]. The presence of alloying elements, mainly Mg, Cu and Fe, form many intermetallics as strengthening precipitates. These intermetallics provide AA2024 with high strength and hardness [3]. However, the intermetallics increase AA2024 susceptiblity to corrosion due to the difference in the potentials of the alloying elements and the Al matrix [4]. The intermetallic particles and the Cu-rich particles formed due to dealloying of $Al_2CuMg$ particles (the S phase) act as effective cathodes and can promote the initiation and growth of pitting corrosion in the matrix. [4]. One of the most common strategies employed to protect metal against corrosion degradation and increase the service life of metallic structures is the application of protective coatings [5-8].

As one of the environmentally friendly coatings for corrosion protection of AA2024-T3 aluminum alloy, hybrid sol-gel coating has been recognized for its good corrosion protective properties [9]. The coating has the advantages of both inorganic networks and organic moieties. The inorganic network provides mechanical properties and good adhesion for the formation of covalent bonds (Si-O-Al) between the matrix and the coating. The organic moiety provides modified properties, such as hydrophobicity and flexibility. The inorganic networks and organic moiety are cross-linked by covalent bonds without a significant phase interface, which assures the dense structure of the coating [10,11]. However, a traditional hybrid sol-gel coating only acts as a passive barrier layer that prevents corrosive media from reaching the metal surface. Various factors, such as mechanical force, temperature shock and corrosive medium, can lead to the formation and growth of defects (pores, cracks, etc.) in the coating and further cause coating degradation and failure. It is necessary to impart active protection to the coating. A common strategy is the use of corrosion inhibitors [12-14]. Nevertheless, the direct introduction of a corrosion inhibitor into the coating would cause detrimental interactions among the coating constituents and the active species of the inhibitor. These interactions lead to the loss of inhibition capability and the formation of coating defects. In addition, the active species are prone to be exhausted quickly the uncontrolled release [15]. Encapsulating corrosion inhibitor into micro/nanocontainers is an effective method to overcome the above disadvantage. Micro/nanocontainer can prevent the direct contact between coating constituent and inhibitor. The failure of protective coating is accompanied by local condition changes at and in the vicinity of the damaged regions. These local changes could be used as intrinsic stimuli for the controlled release of inhibitors from micro/nanocontainers [16]. When inhibitors are released in a controlled manner, they inhibit corrosion processes by reacting with the exposed matrix or forming insoluble matter, etc. [17]. Various kinds of micro/nano materials, such as oxide particles, organic polymers and mesoporous materials, can be used as containers to store corrosion inhibitors [18,19].

As one kind of aluminosilicate material, zeolites contain abundant empty cavities (supercages) and show excellent ion-exchange and adsorption properties. Generally, plentiful $M^{n+}$ exchangeable cations (such as $Na^+$, $K^+$, $Mg^{2+}$, and $Ca^{2+}$) distribute in these supercages [20]. By ion-exchange reactions, inorganic inhibitive cations such as $Co^{2+}$ and $Ce^{3+}$ can be encapsulated into zeolites. It is expected that zeolites filled with inhibitive species would provide controlled release in response to the adsorption of $Mg^{2+}$ and $Cu^{2+}$ from corrosion products, thus increasing the inhibitive capability for the hybrid sol-gel coating [21].

In the present work, a Cobalt-enriched zeolite (CoNaX) synthesized by an ion-exchange reaction of zeolite X (NaX) and $Co(NO_3)_2$ was used as an inhibitor additive to improve the corrosion protection of a hybrid sol-gel coating on AA2024-T3 aluminum alloy. X-ray fluorescence (XRF) spectroscopy, X-ray diffraction (XRD), dynamic light scattering (DLS) and scanning electron microscopy (SEM) were used to characterize the microstructure and constituents of the zeolite particles. Electrochemical impedance spectroscopy (EIS) and potentiodynamic polarization were used to monitor the evolution of the protective properties of the coating.

## 2. EXPERIMENTAL

### *2.1 Materials*

Unclad AA2024-T3 aluminum alloy sheets (50 × 40 × 2 mm) were used as a metallic substrate. The nominal chemical composition was Si, 0.50 wt.%; Cu, 3.80~4.90 wt.%; Fe, 0.50 wt.% ; Mn, 0.30~0.90 wt.%; Mg, 1.20~1.80 wt.%; Zn, 0.25 wt.%; Ti, 0.15 wt.% and Cr, 0.1 wt.% with the balance being Al. Before coating, the sheets were sanded with SiC paper to 2000 grit and washed with distilled water. Then, the sheets were degreased with acetone and etched with 50 $g \cdot L^{-1}$ NaOH solution at 60 °C for 30 s. After rinsing with distilled water, these samples were cleaned with 400 $g \cdot L^{-1}$ aqueous nitric acid ($HNO_3$, $\rho$ = 1.42 $g \cdot ml^{-1}$) for 20 s at room temperature. Finally, the samples were rinsed with distilled water and dried under a hot air stream.

### *2.2 Synthesis of NaX and CoNaX zeolite*

The NaX zeolite was synthesized by the highly efficient crystallization of a seed solution. First, the seed solution was prepared by the following steps. Stoichiometric sodium metaaluminate ($NaAlO_2$) and sodium hydroxide (NaOH) were completely dissolved in deionized water to obtain solution A. Solution A was gradually added into a sodium silicate ($Na_2SiO_3$) solution under vigorous stirring. The mixed solution was sealed and stirred for 30 min, then aged for 24 h at room temperature to obtain the liquid-phase seed solution. The molar composition of $Na_2O$, $Al_2O_3$, $SiO_2$ and $H_2O$ in the liquid-phase seed solution was 15.6: 1: 19: 370, respectively. Subsequently, another aliquot of solution A was added to the as-synthesized liquid-phase seed solution under vigorous stirring. The mixture was sealed and stirred for 1 h. The mixture was poured into a reaction vessel and kept at 100 °C for 16 h to finish the crystallization of NaX zeolite. The molar composition of $Na_2O$, $Al_2O_3$, $SiO_2$ and $H_2O$ in the NaX zeolite was 4.5: 1: 3: 200, respectively. The solid products were washed with deionized water and filtered off before drying in an oven at 100 °C for 24 h.

CoNaX zeolite was prepared by ion-exchange reaction. The obtained NaX zeolite was ultrasonically dispersed in 0.1 M $Co(NO_3)_2$ solution and then the mixture was stirred at 80 °C for 3 h. Next, the solid products were washed 3 times with deionized water and filtered off. The obtained CoNaX zeolite particles were dried in drying oven at 100 °C for 24 h.

### *2.2 Synthesis of sol-gel coating*

Initially, a silane and a zirconium sol were prepared separately. The silane sol was prepared by combining 3-glycidoxypropyl-trimethoxysilane (GPTMS) and anhydrous alcohol in 1.5:1 volume ratio. Then, the mixture was hydrolyzed under vigorous stirring for 1 h by the addition of 0.1 M nitric acid. The molar ratio of water to GPTMS was 5:1. Zirconium sol was obtained by mixing a zirconium n-propoxide (TPOZ, 75 wt.% in n-propanol) precursor with anhydrous alcohol in a 2:1 volume ratio. Acetylacetone (AcAc) was added to the sol as a chelating agent in a 3:1 molar ratio to TPOZ. The zirconium sol was hydrolyzed for 1 h under vigorous stirring by the addition of 0.1 M aqueous nitric

acid solution. The molar ratio of water to TPOZ was 4:1. After that, the two separate sols were mixed under gentle stirring to form hybrid sol. The sol was ultrasonically agitated and stirred for 2 h at room temperature. Then, the sol was divided into several beakers. The $Co(NO_3)_2$, NaX and CoNaX zeolite particles with a 0.05 wt.% concentration were distributed into separate sol beakers under ultrasonic agitation and vigorous stirring. Subsequently, these sols were aged for 12 h and labeled $Co(NO_3)_2$, NaX and CoNaX sols. As a comparison, a sol without an additive was also prepared and labeled Blank sol.

The hybrid sol-gel coating was deposited on the AA2024-T3 aluminum alloy substrates via dipping method. First, the pretreated AA2024 sheets were immersed in $Co(NO_3)_2$, NaX and CoNaX sols. After immersion for 5 min, these sheets were removed at a speed of 180 $mm \cdot min^{-1}$. Subsequently, these sheets were cured in open air for 15 min at room temperature. Finally, the sheets were cured at 110 °C for 1 h in an oven. All sheets were kept in a drying chamber for more than 24 h before use. The prepared coatings were labeled Blank, $Co(NO_3)_2$, NaX and CoNaX coating. Correspondingly, the samples coated by these coatings were labeled Blank, $Co(NO_3)_2$, NaX and CoNaX samples.

### *2.3 Characterization*

The proportion of Co in CoNaX zeolite was measured by XRF (XRF-1800, Japan). The crystalline structure of zeolites was characterized by XRD (D-AMX2500, Japan) with Cu$K_\alpha$ ($\lambda$=0.15418 nm) radiation, operating at 40 kV and 200 mA. The data were collected in the 2θ range from 5° to 50° at a scan rate of $2° \cdot min^{-1}$. The microstructure of zeolite particles and sol-gel coatings were studied by SEM (JEOL JSM-7500, Japan). The specific surface area measurements of zeolite particles were carried out by the Brunauer-Emmett-Teller (BET) method. After aging for 12 h at room temperature, particle size measurements were carried out by DLS using a particle size instrument (Malvern Zetasizer Nano S, UK). Fourier transform infrared (FTIR) spectra for sol-gel coatings were recorded by a Nicolet NEXUS 470 spectrometer in the range from 4000 to 400 $cm^{-1}$ with a resolution of 4 $cm^{-1}$. Electrochemical impedance spectroscopy (EIS) and potentiodynamic polarization were performed on a PARSTAT 2273 electrochemical workstation (Princeton Applied Research, USA) with a three-electrode system in 0.05 M NaCl aqueous solution at 25 °C. A low concentration of the NaCl aqueous solution was used to decrease the rate of corrosion processes and improve estimation of the processes in the early stages. A saturated calomel electrode (SCE) was used as the reference electrode (RE), and a platinum plate was used as the counter electrode (CE). The exposed area of the working electrode (WE) was 1 $cm^2$. EIS data were recorded in range of $10^5$ ~$10^{-2}$ Hz with 10 mV sinusoidal perturbations at an open circuit potential (OCP) after different immersion times. Potentiodynamic polarization plots were scanned from -0.25 V to +0.25 V (vs. OCP) with a scan rate of 1 $mV \cdot s^{-1}$. At least three samples were tested for each type of coating to ensure the reproducibility of results.

## 3. RESULTS AND DISCUSSION

### *3.1 Characterization of NaX and CoNaX zeolite*

A synthesis schematic of the CoNaX zeolite is presented in Fig. 1. $Na^+$ cations in the NaX zeolite

were exchanged with $Co^{2+}$ cations by ion-exchange reactions. The XRF results confirm a Co concentration of 15.1 wt.% in the CoNaX zeolite. SEM micrographs of NaX and CoNaX zeolites are depicted in Fig. 2. The morphology of the CoNaX zeolite is similar to that of the NaX zeolite. The particle sizes are both approximately 50 nm. This implies that the ion-exchange reaction does not cause significant changes in zeolite shape. In addition, the specific surface area of the NaX zeolite determined by BET analysis is 457.0 $m^2 \cdot g^{-1}$ and the surface area of the CoNaX zeolite decreased slightly to 425.6 $m^2 \cdot g^{-1}$. The slight changes in specific surface area suggest that the ion-exchange reaction will not damage the supercage structure of NaX zeolite.

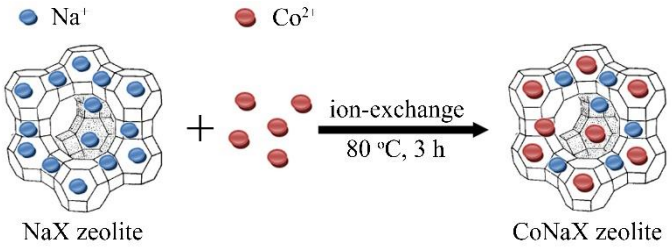


**Figure 1.** Synthesis of CoNaX zeolite by dispersing NaX zeolite in 0.1 M $Co(NO_3)_2$ solution (ion-exchange reaction of $Na^+$ and $Co^{2+}$) at 80 °C for 3 h under stirring.

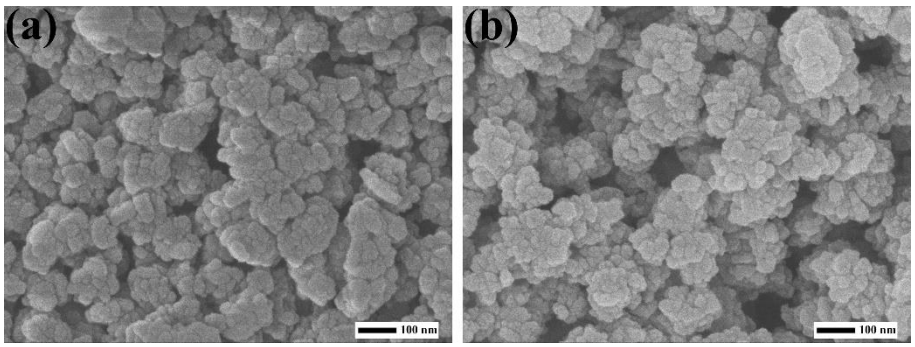


**Figure 2.** SEM micrograph of (a) NaX and (b) CoNaX zeolites. The particle sizes are both approximately 50 nm.

Fig. 3 shows XRD patterns of the as-synthesized NaX and CoNaX zeolites. As a comparison, the standard diffraction pattern of NaX zeolite (JCPDS: 38-0237) is shown as well. The characteristic diffraction peaks of the NaX and CoNaX zeolites are in good conformity with the standard diffraction pattern. It indicates that the NaX zeolite is prepared successfully and that the ion-exchange of $Co^{2+}$ with $Na^+$ does not change the crystal structure of the NaX zeolite.

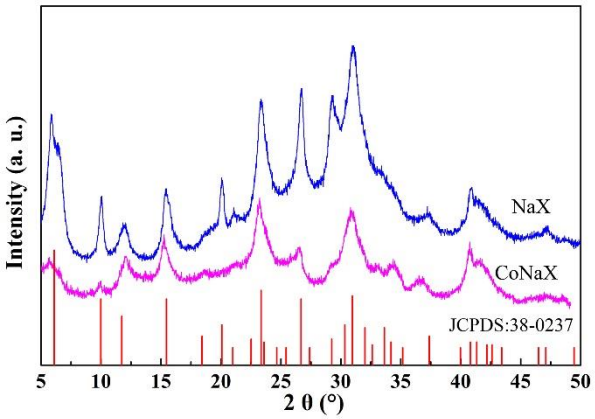


**Figure 3.** XRD patterns of the as-synthesized NaX (blue) and CoNaX (pink) zeolites and the standard diffraction pattern (red) of zeolite (JCPDS: 38-0237) at 25 °C.

*3.2 Sol synthesis and DLS characterization*

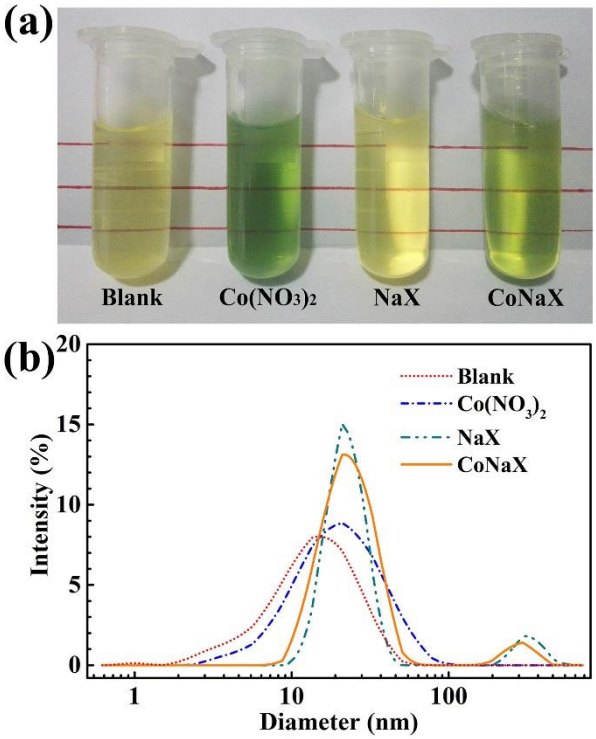


**Figure 4.** Digital images (a) and particle size distribution (b) of the as-prepared Blank (red) and doped with $Co(NO_3)_2$ (blue), NaX (wathet-blue) and CoNaX (orange) hybrid sols.

A transparent light-yellow sol is obtained by mixing two separate sols under gently stirring, as shown in Fig. 4a. The addition of $Co(NO_3)_2$, NaX and CoNaX changes the sol color. These sols remain transparent and no clear gelation occurs for several weeks in sealed storage at room temperature. The curves of particle size distribution of these as-prepared sols after aging for 12 h at room temperature are shown in Fig. 4b. One peak distribution is observed for Blank and $Co(NO_3)_2$ sols, suggesting that these two sols are homogeneous. The addition of $Co(NO_3)_2$ leads to an increase in particle size (from ~12.7

nm to 23 nm). In contrast, the sols with zeolites show a bimodal distribution at ~20 and ~300 nm. The peak at ~300 nm is ascribed to the linked zeolite particles (approximately 5~6 zeolite particles), which suggested that there is no clear agglomeration in the sol. These curves indicate that the both zeolites disperse uniformly in the sols and that zeolite is suitable for sol-gel coating system.

### *3.3 Corrosion inhibition efficiency of the CoNaX zeolite*

The corrosion inhibitory property of the synthesized CoNaX zeolite was assessed by immersing bare AA2024 into a plain 0.05 M NaCl solution and a 0.05 M NaCl solution doped with CoNaX zeolite (5 $g \cdot L^{-1}$). Fig. 8 depicts EIS curves and polarization curves of bare AA2024 after immersion for 5 h in different solutions. EIS curves show that the impedance of the sample in the presence of CoNaX zeolite shows much higher values than that of the samples in the plain NaCl solution. Polarization curves show that the presence of CoNaX zeolite decreases the corrosion potential ($E_{corr}$). That is attributed to the activated surface by released $Co^{2+}$. The corrosion current densities ($I_{corr}$) of bare AA2024-T3 decreases synchronously. In addition, the sample in the presence of CoNaX shows a higher anode slope and lower anodic current density, suggesting the suppression of the anodic dissolution process. These results indicate that the $Co^{2+}$ is released from the CoNaX zeolite in a NaCl solution and inhibits the corrosion of bare AA2204.

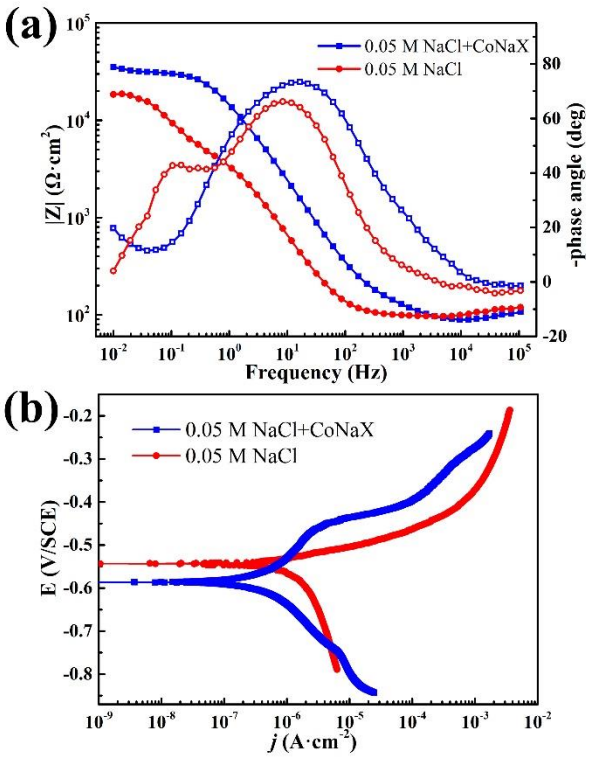


**Figure 5.** EIS curves (a) and polarization curves (b) of bare AA2024 after immersion for 5 h in 0.05 M NaCl solution (red) and in 0.05 M NaCl solution with CoNaX zeolite (blue) at 25 °C.

*3.3 Characterization of sol-gel coating*

The Blank, $Co(NO_3)_2$, NaX and CoNaX coatings are all transparent, colorless and free of macroscopic cracks to naked eyes. Fig. 6 depicts the SEM micrograph of these coatings. All coatings are continuous, smooth and crack-free, and completely cover the alloy substrate. No agglomerated zeolite is detected on the surface of the NaX and CoNaX coatings. That implies that both zeolites distribute homogeneously without causing defects, suggesting the good compatibility of this kind of zeolite with a sol-gel coating. Fig. 7 shows an SEM micrograph of a cross section of the four coatings. The average thickness of the coatings is 2.2 ± 0.2 µm. The addition of zeolite causes unclear increase in coating thickness.

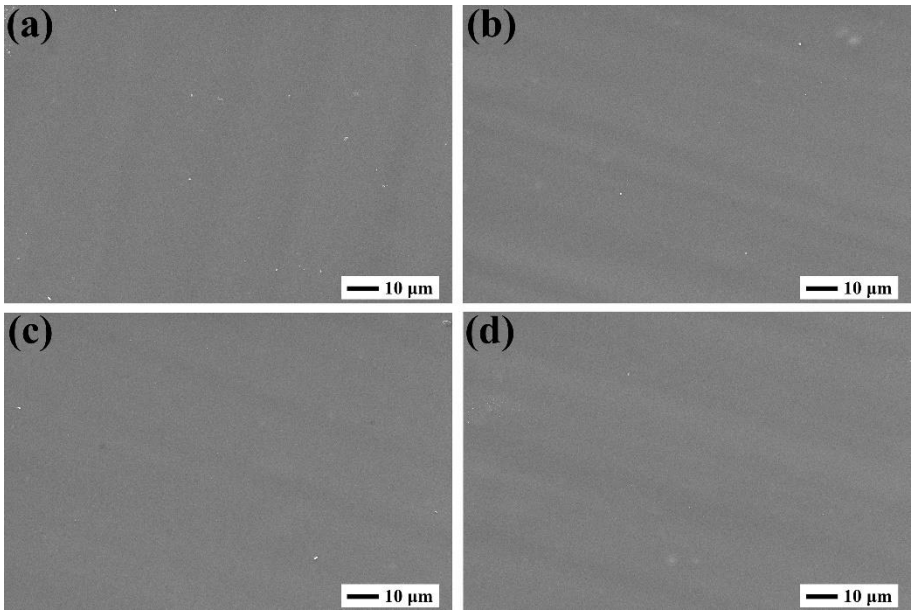


**Figure 6.** SEM micrograph of the Blank (a) and doped with $Co(NO_3)_2$ (b), NaX (c) and CoNaX (c) coatings.

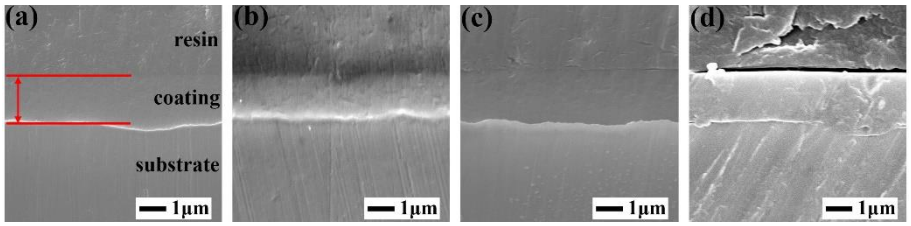


**Figure 7.** SEM micrograph of the cross sections of the Blank (a) and doped with $Co(NO_3)_2$ (b), NaX (c) and CoNaX (c) coatings.

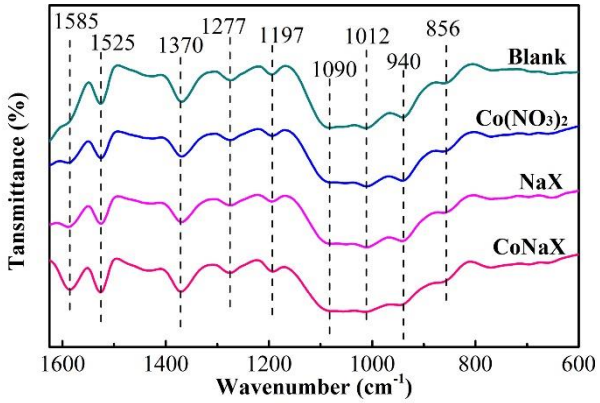


**Figure 8**. FTIR spectra of Blank (wathet-blue), $Co(NO_3)_2$ (blue), NaX (pink) and CoNaX (red) coatings

FTIR spectra of Blank, $Co(NO_3)_2$, NaX and CoNaX coatings are depicted in Fig. 8. The bands at ~1012 and ~1090 $cm^{-1}$ correspond to the Si-O-Si bond asymmetric stretching vibration, confirming the formation of network structure in the hybrid sol-gel coatings [22,23]. The bond at ~1197 $cm^{-1}$ is the characteristic peak of C-O-C in the epoxy functional group from GPTMS. The peak at 940 $cm^{-1}$ is attributed to rocking vibrations of the Si-C bond from GPTMS [11]. The absorption bands located at ~856 $cm^{-1}$ are related to Si-O-Zr bonds, which results from the heterocondensation between the Si-OH and Zr-OH groups [24]. Two sharp peaks at ~1585 and ~1525 $cm^{-1}$ correspond to Zr/AcAc chelating ligands [5]. The increased intensity of sharp peaks at ~1585 $cm^{-1}$ implies that the zeolite particles influence the complicated chelation reaction and participate in the formation of sol-gel coatings.

### *3.4 Electrochemical measurements of sol-gel coating*

Electrochemical measurements were employed to study and compare the corrosion inhibition effect of $Co(NO_3)_2$, NaX and CoNaX zeolites. The potentiodynamic polarization curves of samples after immersion for 1 h and 168 h in 0.05 M NaCl solution are shown in Fig. 9. The results of the Tafel extrapolation of the polarization curves are presented in Table 1 [25,26]. The addition of additives decreases the $E_{corr}$ of these coated samples, while there is no significant difference in the $I_{corr}$ after immersion for 1 h. This is ascribed to the fact that these samples undergo decreased onset corrosion at the beginning of immersion and that the protective properties of the coatings rely on an ant-corrosion barrier for the coating integrity. The additive doped samples show better corrosion resistance due to having lower $I_{corr}$ values than the Blank sample. The cathodic branch of the polarization curves givse rise to unparallel lines and the CoNaX sample presents significantly smaller current density. The results reveal that the addition of CoNaX suppresses the hydrogen evolution reaction in cathodic areas. Similarly, the CoNaX sample also shows a lower anodic current density, suggesting the suppression of the anodic dissolution process ($Al - 3e + Al^{3+}$) [27].

After immersion for 168 h, the corrosion resistance of the Blank and $Co(NO_3)_2$ samples decreases significantly due to the rapid increase in $I_{corr}$ and the decrease in $E_{corr}$. Compared with the Blank coating, the $Co(NO_3)_2$ coating shows similar protective properties. This behavior is attributed to the

uncontrollable release of corrosion inhibitors ($Co^{2+}$), which leads to a quick loss of the self-healing property during long-term immersion. In contrast, the CoNaX coating reveals excellent long-term protective properties. The $I_{corr}$ of the CoNaX sample is one order of magnitude lower than that of the Blank sample. The good protective property of the CoNaX coating is attributed to two factors. First, zeolite particles, as reinforcements, enhance the cross-linking density of the sol-gel coatings by covalent reactions with silane precursors. This line of reasoning is confirmed by the NaX coating having better protective property than the Blank coating. Second, the zeolite plays the role of nanocontainers to store inhibitors, which ensures the controllable release of $Co^{2+}$ when a defect is formed in the coating. It is beneficial to provide long-term self-healing properties.

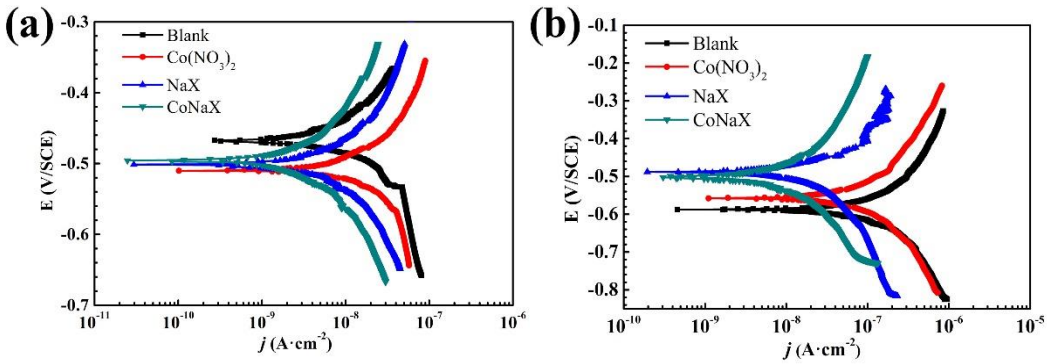


**Figure 9.** Polarization curves of Blank (black), $Co(NO_3)_2$ (red), NaX (blue) and CoNaX (wathet-blue) coatings after immersion for 1 h (a) and 168 h (b) in 0.05 M NaCl solution at 25 °C.

**Table 1.** Corrosion parameters for bare AA2024-T3 alloy and sol-gel coatings in 0.05 M NaCl solution determined by the Tafel extrapolation method

| Immersion time | Parameter | Blank | $Co(NO_3)_2$ | NaX | CoNaX |
|---|---|---|---|---|---|
| 1 h | $i_{corr}$ ($A \cdot cm^{-2}$) | $8.38\times10^{-9}$ | $1.14\times10^{-8}$ | $5.46\times10^{-9}$ | $3.89\times10^{-9}$ |
| | $E_{corr}$ (V) | -0.469 | -0.509 | -0.502 | -0.495 |
| 168 h | $i_{corr}$ ($A \cdot cm^{-2}$) | $1.20\times10^{-7}$ | $1.05\times10^{-7}$ | $3.53\times10^{-8}$ | $1.31\times10^{-8}$ |
| | $E_{corr}$ (V) | -0.558 | -0.588 | -0.498 | -0.501 |

The EIS measurements of these samples were performed during 336 h of immersion in 0.05 M NaCl solution. The selected representative Bode plots obtained after immersion for 1 h, 72 h, 216 h and 336 h are depicted in Fig. 10. Generally, the impedance values at low frequencies ($|Z|_{0.01Hz}$) reflect the protective properties of the coating [28]. After 1 h of immersion (Fig. 10a), $|Z|_{0.01Hz}$ values of $Co(NO_3)_2$, NaX and CoNaX coatings are higher than those of the Blank coating. The addition of these additives improves the protective properties of the sol-gel coatings in the initial immersion period. The CoNaX coating shows an improved protective property with the highest $|Z|_{0.01\ Hz}$ value of $2.58 \times 10^6\ \Omega \cdot cm^2$. The impedance values for all samples decrease with immersion time due to the permeation of the electrolyte. After immersion for 72 h, the impedance of Blank and $Co(NO_3)_2$ samples show a significant decrease.

The $|Z|_{0.01\ Hz}$ value of the $Co(NO_3)_2$ sample decreases to less than $10^6\ \Omega \cdot cm^2$ (Fig. 10b). Although the addition of $Co(NO_3)_2$ improve the protective properties of the sol-gel coating, the effect is lost quickly because of the uncontrollable release of $Co^{2+}$. The corrosion inhibitor is used up during the initial immersion. In contrast, the $|Z|_{0.01\ Hz}$ values of the NaX and CoNaX samples remain higher than $10^6\ \Omega \cdot cm^2$, indicating that the addition of zeolites can delay the deterioration of the sol-gel coatings. This might be due to the improved cross-linking density of the sol-gel coating by the zeolite particles and the controllable release of $Co^{2+}$ from the zeolites. This is confirmed by the CoNaX coating having better protective properties than the NaX coating. After immersion for 216 h (Fig. 10c), the impedance of the $Co(NO_3)_2$ sample is similar to that of the Blank sample, implying that the effect of $Co(NO_3)_2$ has been lost. In contrast, the CoNaX coating reveals much increased impedance values at low and intermediate frequencies. In addition, the resistive plateaus of impedance move to higher frequencies after immersion for 336 h, as shown in Fig. 10d. This suggests the breakdown of these coatings.

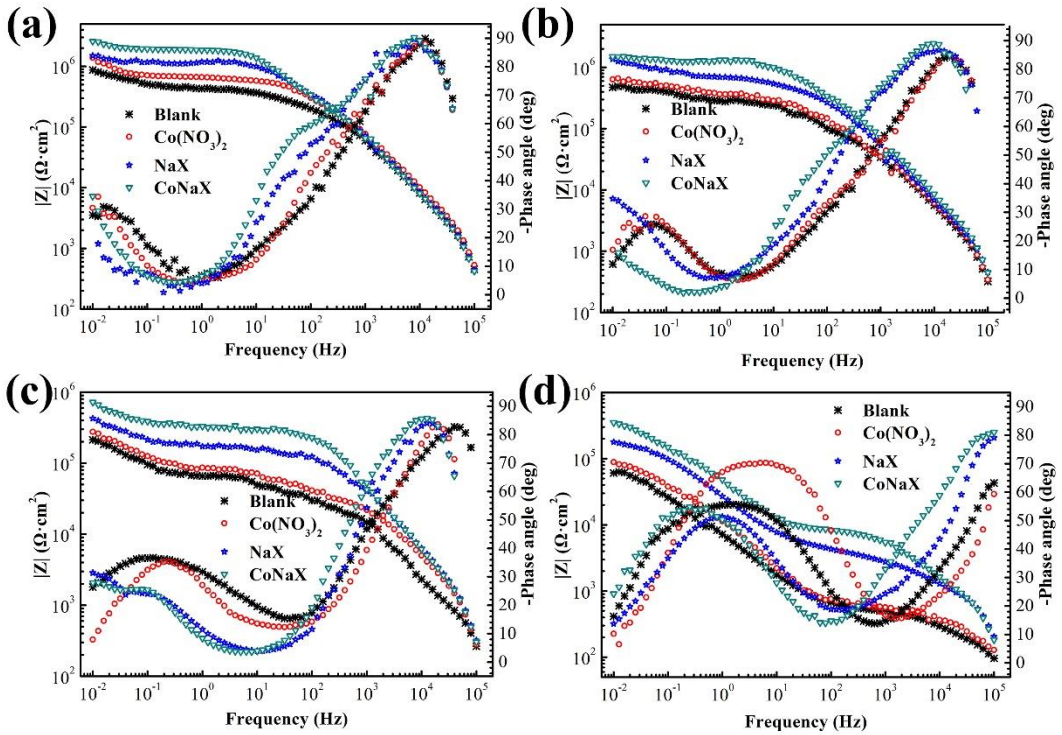


**Figure 10.** Bode plots of Blank (black), $Co(NO_3)_2$ (red), NaX (blue) and CoNaX (wathet-blue) coatings after immersion for 1 h (a), 72 h (b), 216 h (c) and 336 h (d) in 0.05 M NaCl solution at 25 °C.

In the early stage, two time constants are observed at ~$10^4$ and ~0.5 Hz in the Bode-phase plots. They are assigned to capacitances of the coating ($C_{coat}$) and intermediate oxide layer ($C_{oxide}$), respectively. A third time constant related to onset corrosion appears at low frequencies (~0.05) for the Blank and $Co(NO_3)_2$ samples after immersion for 72 h, implying poor corrosion protection of these two coatings and the presence of substrate corrosion [29]. The third time constant is attributed to the double layer capacitance ($C_{dl}$) of the corroded areas. Additionally, the three resistances observed in Bode impedance

plots are the resistance of the coating pore ($R_{pore}$) and intermediate oxide layer ($R_{oxide}$) along with the polarization resistance ($R_{polar}$) of double layer capacitance [30]. In addition, the resistance of solution ($R_{sol}$) is observed at $10^5$ Hz in Bode-impedance plots. After long-term immersion (216 h and 336 h), the third time constant for NaX and CoNaX samples in Bode-phase plots appears, suggesting substrate corrosion.

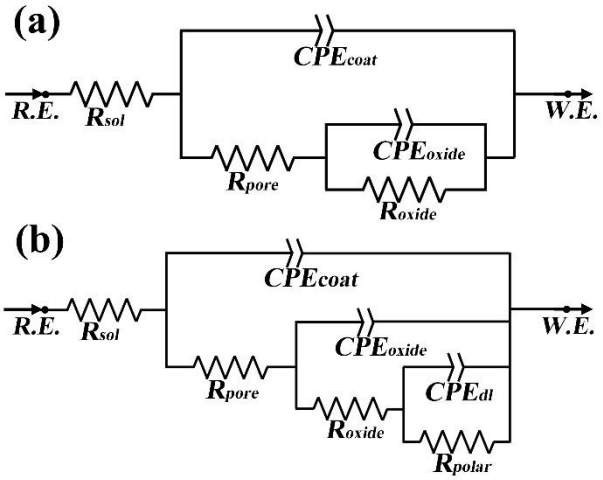


**Figure 10.** Equivalent circuit (EC) used to fit the experimental EIS data. EC (a): before the appearance of corrosion; EC (b): after the appearance of corrosion.

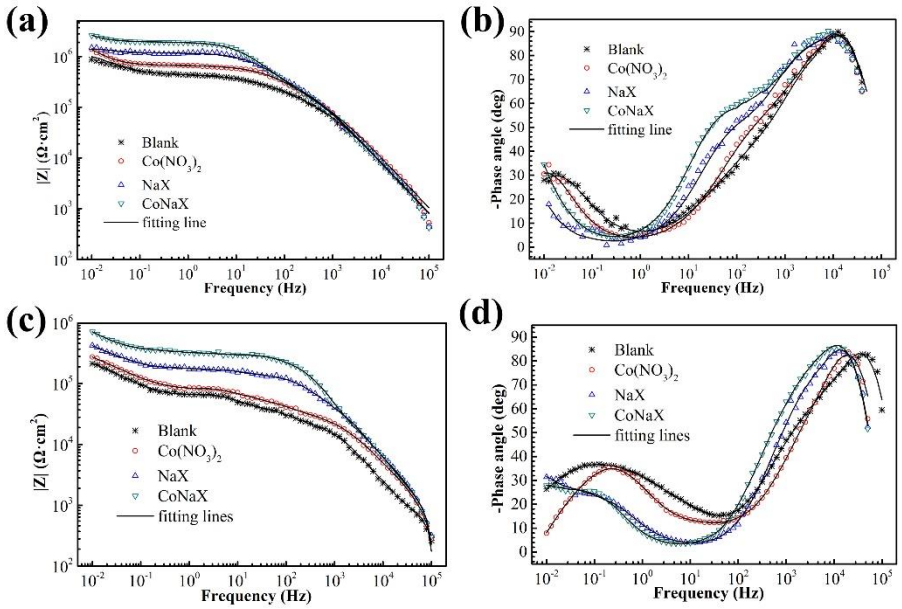


**Figure 11.** EIS data (point) and the fitting results (lines) of coatings after immersion for 1 h (a, b) and 216 h (c, d) in 0.05 M NaCl solution at 25 °C.

For quantitative interpretation of the physicochemical behavior of sol-gel coatings during

immersion, the EIS results are simulated by numerical fitting using the equivalent circuit presented in Fig. 10. In these models, it is considered that the electrochemical behavior of the systems does not correspond to pure capacitors; therefore, the constant phase elements $CPE_{coat}$, $CPE_{oxide}$ and $CPE_{dl}$ are used instead of the three capacitances. Before the appearance of corrosion, the EIS results are fitted by using the equivalent circuit model presented in Fig. 10a. The equivalent circuit model shown in Fig. 10b is used when a third time constant related to onset corrosion appears. The chi-squared error of fitting is less than $10^{-3}$ for all the spectra. Fig. 11 depicts the results of fitting the data from these samples after 1 h by model (a) and the results from fitting the data from these samples after 216 h by model (b).

The evolution of $R_{pore}$ and $R_{oxide}$ from the fitting result during 336 h of immersion in 0.05 M NaCl solution are depicted in Fig. 12. Due to the corrosive species penetration via pore and microcrack in the sol-gel network, the decrease in $R_{pore}$ with increasing time indicates coating deterioration [31]. Compared with the zeolite doped sol-gel coatings, the Blank and $Co(NO_3)_2$ coatings show a rapid decrease in $R_{pore}$ with a low value approximately $3 \times 10^2$ Ω·cm$^2$ at the end of immersion. The $Co(NO_3)_2$ coating shows similar $R_{pore}$ values as the Blank coating during the whole immersion period. This suggests that the $Co(NO_3)_2$ addition does not cause drastic improvement in the protective properties of the sol-gel coating. In contrast, the $R_{pore}$ for zeolite doped sol-gel coatings is high in the early stage and decrease slowly, especially for the CoNaX coating. The $R_{pore}$ values of the CoNaX coating are stable with long-term immersion. After 336 h of immersion, the $R_{pore}$ value of the CoNaX coating is more than two orders of magnitude higher than that of the Blank coating. The stable $R_{pore}$ is attributed to the enhanced cross-linking density and the controllable release of $Co^{2+}$ from the CoNaX zeolite.

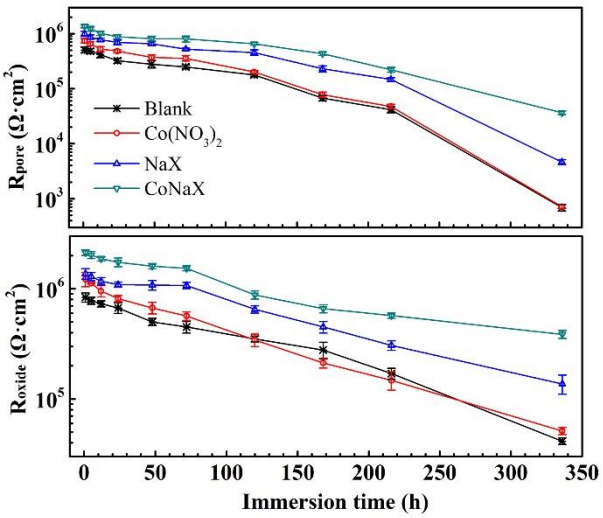


**Figure 12.** Evolution of the resistance of the coating pore ($R_{pore}$) and intermediate oxide layer ($R_{oxide}$) during 336 h of immersion in 0.05 M NaCl solution at 25 °C.

The intermediate oxide layer is composed of native aluminum oxide and Al-O-Si or Al-O-Zr covalent bonds formed by the interaction of Al-OH groups with Si-OH or Zr-OH [32]. This layer is the last barrier between the aggressive species and the aluminum alloy substrate. The compactness and

integrity of the layer are of great importance. The defects in the layer allow the direct penetration of aggressive species to the alloy substrate causing corrosion activities. As shown in Fig. 12, the addition of zeolite increases the $R_{oxide}$ values, implying the formation of a more compact oxide layer. The CoNaX coating possesses the highest $R_{oxide}$ values with the immersion period and the decrease in the $R_{oxide}$ of CoNaX is much slower compared with that of NaX coating. Even after 336 h of immersion, the CoNaX coating shows a $R_{oxide}$ of approximately $4 \times 10^5$ $\Omega \cdot cm^2$. It contributes to the effect of controllable release of $Co^{2+}$ in the CoNaX zeolite. $Co^{2+}$ reacts with $OH^-$ from the corrosion products and forms Co oxide/hydroxide precipitation. The precipitation repairs the defects in the intermediate oxide layer.

### *3.5 Immersion test*

Optical photographs of these sol-gel coatings after 336 h of immersion in 0.05 M NaCl solution are shown in Fig. 13. The Blank and $Co(NO_3)_2$ samples undergo a more severe onset corrosion with higher pitting site densities and dull gray colors. Only a few pitting sites can be observed on the NaX samples, indicating the improved corrosion protective properties of the NaX coating. In contrast, the CoNaX sample retains an almost undamaged substrate.

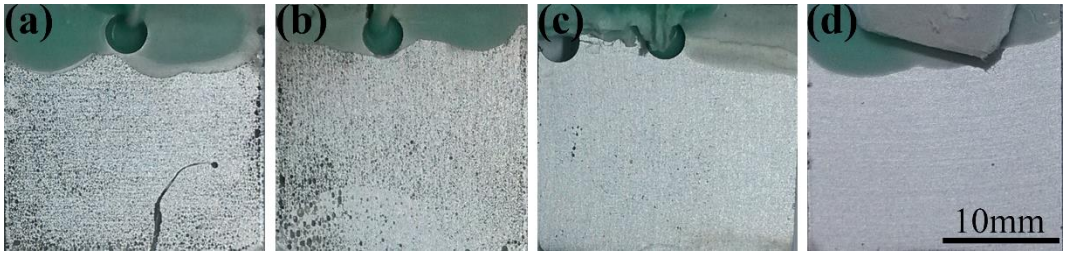


**Figure 13**. Optical photographs of the coated samples after 336 h of immersion in 0.05 M NaCl solution at 25 °C. (a) Blank; (b) $Co(NO_3)_2$; (c) NaX; and (d) CoNaX coatings

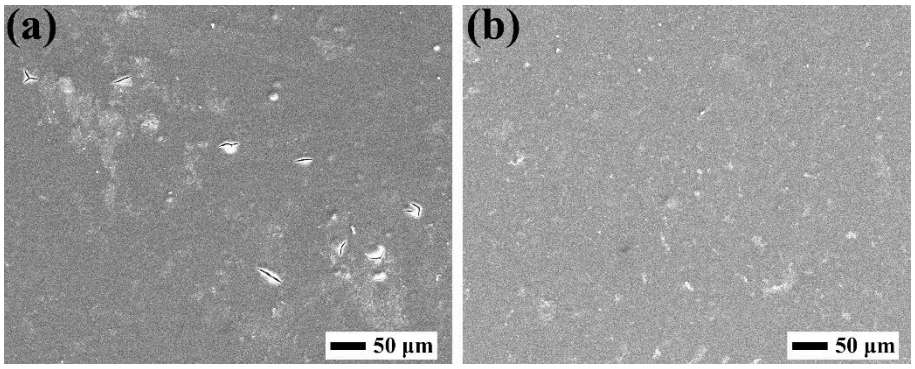


**Figure 14.** SEM micrographs of (a) NaX and (b) CoNaX samples after 336 h of immersion in 0.05 M NaCl solution at 25 °C.

To improve the distinction, the micromorphology of these coatings was determined by SEM. As shown in Fig. 14a, typical cracks appear on the surface of the NaX coating. However, during the same immersion period, the CoNaX coating retains its integrity without clear cracks on the surface (Fig 14b).

The results reveal that the addition of CoNaX zeolites improves the barrier properties of the coating and confers active corrosion protection to the AA2024 substrate, in agreement with the results of the electrochemical measurements.

### *3.6 Corrosion inhibition mechanism*

Fig. 15 depicts a schematic representation of the $Co^{2+}$ release process and the formation of a Co oxide/hydroxide precipitate in a sol-gel coating defects. After contact with the corrosive environment, the corrosion medium penetrates the protective coating and comes in contact with the intermetallic surface ($Al_2CuMg$, especially) causing the chemical reactions of active aluminum and magnesium with water [29]:

$$Al \rightarrow Al^{3+} + 3e \quad (1)$$

$$Mg \rightarrow Mg^{2+} + 2e \quad (2)$$

$$O_2 + 2H_2O + 4e \rightarrow 4OH^- \quad (3)$$

Dealloying of these intermetallics leads to a local increase in pH around the particles and enrichment of their surface with copper, which results in shifting the dissolution processes from chemical to electrochemical [29,33]. Meanwhile, $Co^{2+}$ is released via ion-exchange reactions with the generated $Mg^{2+}$ or $Al^{3+}$.

The further increase in pH in the corrosion regions leads to the reaction of $OH^-$ with the released $Co^{2+}$ and formation of a Co oxide/hydroxide precipitation according to the following reactions [3]:

$$Co^{2+} + 2OH^- \rightarrow Co(OH)_2 \downarrow \quad (4)$$

The precipitation products can cover the defects, thus preventing the contact of the electrolyte with the substrate and retarding the corrosion process [34]. CoNaX can overcome the negative effects of direct inhibitor addition. The controllable release of inhibitors from the zeolites results in sustained corrosion protection for the alloy substrate.

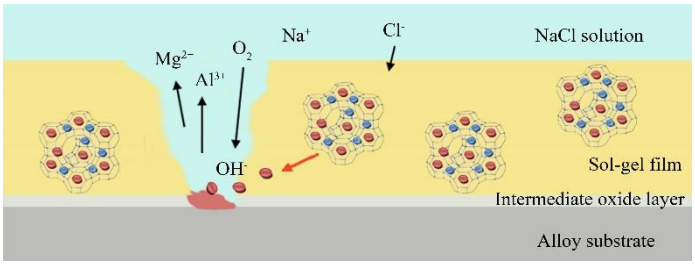


**Figure 15.** Schematic diagram of the release process of $Co^{2+}$ and the formation of a Co oxide/hydroxide precipitate in the defect.

## 4. CONCLUSIONS

NaX zeolite was used as an ion-exchanger to prepare Cobalt-enriched zeolite reservoirs via ion-

exchange reactions. The obtained CoNaX zeolite was introduced into a hybrid sol-gel system to prepare a self-healing sol-gel coating. The zeolite particles dispersed uniformly in the sol-gel coatings without causing defects in the coating or a significant increase in the thickness. The CoNaX zeolite remarkably improved the corrosion protective properties of the sol-gel coating and provided the coating with long-term self-healing properties. Even after 336 h of immersion, the CoNaX coating retained its integrity without clear cracks on the surface. These features were attributed to an enhanced cross-linked density and a controllable release of $Co^{2+}$ from the CoNaX zeolite. The $Co^{2+}$ reacted with the $OH^-$ from corrosion products and formed Co oxide/hydroxide precipitates. The precipitation products covered the defects and prevented contact of the electrolyte with the substrate. As a result, the corrosion processes were slowed.

ACKNOWLEDGMENTS
This work was supported by the Natural Science Foundation of Jiangsu Province of China (NO.: BK20180176).

## References

1. M. Schem, T. Schmidt, J. Gerwann, M. Wittmar, M. Veith, G.E. Thompson, I.S. Molchan, T. Hashimoto, P. Skeldon, A.R. Phani, S. Santucci, M.L. Zheludkevich, *Corros. Sci.*, 51 (2009) 2304.
2. R. Naderi, M. Fedel, F. Deflorian, M. Poelman, M. Olivier, *Surf. Coat. Tech.*, 224 (2013) 93.
3. K.A. Yasakau, M.L. Zheludkevich, S.V. Lamaka, M.G.S. Ferreira, *J. Phys. Chem. B*, 110 (2006) 5515.
4. H. Zhao, M. Yu, J. Liu, S. Li, B. Xue, *J. Electrochem. Soc.*, 164 (2017) C641.
5. M. Yu, M. Liang, J. Liu, S. Li, B. Xue, H. Zhao, *Appl. Surf. Sci.*, 363 (2016) 229.
6. D. Fix, D.V. Andreeva, Y.M. Lvov, D.G. Shchukin, H. Möhwald, Application of Inhibitor-Loaded Halloysite Nanotubes in Active Anti-Corrosive Coatings, *Adv. Funct. Mater.*, 19 (2009) 1720.
7. T. Stimpfling, F. Leroux, H. Hintze-Bruening, *Colloids Surf. A Physicochem. Eng. Asp.*, 458 (2014) 147.
8. Shixian Zhang, Yungang Li, Cong Wang, Xiaoping Zhao, *Int. J. Electrochem. Sci.*, 14 (2019) 91.
9. M. Yu, B. Xue, J. Liu, S. Li, Y. Zhang, *Thin Solid Films*, 590 (2015) 33.
10. Y. Liu, D. Sun, H. You, J.S. Chung, *Appl. Surf. Sci.*, 246 (2005) 82.
11. R.G. Wankhede, S. Morey, A.S. Khanna, N. Birbilis, *Appl. Surf. Sci.*, 283 (2013) 1051.
12. M. Yu, Y. Liu, J. Liu, S. Li, B. Xue, Y. Zhang, X. Yin, *Chinese J. Aeronau*t., 28 (2015) 600.
13. A.C. Balaskas, I.A. Kartsonakis, D. Snihirova, M.F. Montemor, G. Kordas, *Prog. Org. Coat.*, 72 (2011) 653.
14. H. Lgaz, R. Salghi, Ismat H. Ali, *Int. J. Electrochem. Sci.*, 13 (2018) 250.
15. L. Songmei, Y. Xiaolin, L. Jianhua, Z. You, X. Bing, *Acta Phys-chim. Sin.*, 30 (2014) 2092.
16. Jun Cui, Xiuqing Li, Zhiqiang Pei, Yuansheng Pei, *Chem. Eng. J.*, 358 (2019) 379.
17. D. Borisova, H. Möhwald, D.G. Shchukin, *Acs Appl. Mater. Inter.*, 4 (2012) 2931.
18. D. Snihirova, S.V. Lamaka, M.F. Montemor, *Electrochim. Acta*, 83 (2012) 439.
19. D. Álvarez, A. Collazo, M. Hernández, X.R. Nóvoa, C. Pérez, *Prog. Org. Coat.*, 68 (2010) 91.
20. G.T. Palomino, S. Bordiga, A. Zecchina, G.L. Marra, C. Lamberti, *J. Phys. Chem. B*, 104 (2000) 8641.
21. S. Dias, S.V. Lamaka, T.C. Diamantino, M. Ferreira, *J. Electrochem. Soc.*, (2014) C215.
22. L. Chen, H. Jin, Z.W. Xu, M.J. Shan, X. Tian, C.Y. Yang, Z. Wang, B.W. Cheng, *Mater. Chem. Phys.*, 145 (2014) 186.

23. M. Izadi, T. Shahrabi, B. Ramezanzadeh, *Appl. Surf. Sci.*, 440 (2018) 491.
24. E. Cordoncillo, J. Carda, H. Beltran, F.J. Guaita, A. Barrio, P. Escribano, B. Viana, C. Sanchez, *Bol. Soc. Esp Ceram. V*, 39 (2000) 95.
25. N. Zidane, Y. Ait Albrimi, A. Ait Addi, J. Douch, R.M. Souto, M. Hamdani, *Int. J. Electrochem. Sci.*, 13 (2018) 29.
26. H. Rahmani, K. Ismaily Alaoui, K.M. Emran, A. El Hallaoui, M. Taleb, S. El Hajji, B. Labriti, E. Ech-chihbi1, B. Hammouti, F. El-Hajjaji, *Int. J. Electrochem. Sci.*, 14 (2019) 985.
27. S. John, A. Joseph, *Rsc. Adv.*, 2 (2012) 9944.
28. W. Sun, L. Wang, T. Wu, M. Wang, Z. Yang, Y. Pan, G. Liu, *Chem. Mater.*, 27 (2015) 2367.
29. M.L. Zheludkevich, R. Serra, M.F. Montemor, K.A. Yasakau, I.M.M. Salvado, M.G.S. Ferreira, *Electrochim. Acta*, 51 (2005) 208.
30. Xiaodong Zhao, Kefeng Chen, Jie Yang, Guangfeng Xi, Haitao Tian, Qingguo Chen, *Int. J. Electrochem. Sci.*, 14 (2019) 875.
31. K.A. Yasakaua, A. Kuznetsova, S. Kallipa, M. Starykevich, J. Tedim, M.G.S. Ferreira, M.L. Zheludkevich, *Corros. Sci.*, 143 (2018) 299.
32. M. Quinet, B. Neveu, V. Moutarlier, P. Audebert, L. Ricq, *Prog. Org. Coat.*, 58 (2007) 46.
33. P. Rodic, I. Milosev, *J. Electrochem. Soc.*, 162 (2015) C592.
34. Fan Zhang, Pengfei Ju, Mengqiu Pan, Dawei Zhang, Yao Huang, Guoliang Li, Xiaogang Li, *Corros. Sci.*, 144 (2018) 74.